Fracture of Type 347 stainless steel

by

Thomas Mason Parker

A Thesis Submitted to the
Graduate Faculty in Partial Fulfillment of
The Requirements for the Degree of
MASTER OF SCIENCE

Major Subject: Nuclear Engineering

Iowa State University
Ames, Iowa

1971

INTRODUCTION

The objective of this research was to correlate the microstructure of AISI Type 347 stainless steel with fracture mechanisms. This information will assist in extending an understanding of how and why stainless steel fractures. There are four mechanisms of fracture: plastic deformation, cleavage, creep and fatigue fracture. Plastic deformation fracture was studied in this research. Type 347 stainless steel (347ss) was used because of its importance in Nuclear Engineering.

The Nuclear industry has a large need for corrosion resistant material in nuclear reactors and reprocessing plants. Stainless steels have good strength, ductility and corrosion resistance. In many situations it is desirable to weld the material. Type 347ss was designed especially for welding. One of the problems of welding other stainless steels is that chromium carbides precipitate during welding. If the chromium is tied up in the form of carbides, the area loses its corrosion resistance. Type 347ss prevents chromium carbides from forming by adding niobium which combines with the carbon. The chromium is left unaffected and corrosion resistance is not impaired.

The microstructure was studied in two states: undeformed and deformed. The undeformed state was studied by observing polished surfaces. Inclusions and second phase particles were studied in the polished surface. Size, shape and chemical

information was needed for these inclusions and second phase particles.

In the deformed state, fracture mechanics and information on microstructure were obtained. Polished and fresh fracture surfaces were studied. Samples were deformed until necking occurred and were then cut, mounted and polished. This was done to find information about inclusions or second phase particles and their relation to possible void formation. Size, shape and chemical information was needed here. Topographical and chemical information was obtained from fracture surfaces.

The macroscopic and microscopic properties affect one another, and in order to study one, the other must be studied. Hardness, strength, chemical information, the sample history and macroscopic properties, would be necessary to characterize the samples.

After studying the deformed and undeformed states it would then be possible to correlate the information from the two states. From this it was hoped that a better understanding of fracture of stainless steel would result.

LITERATURE REVIEW

Macrostructure of Type 347 Stainless Steel

The major components of Type 347ss are iron (Fe), chromium (Cr), and nickel (Ni). Other significant components present in smaller amounts are carbon (C), manganese (Mn), phosphorus (P), silicon (Si), sulfur (S), niobium (Nb), aluminum (Al), and oxygen (O). Type 347ss is an aluminum killed steel, which means that aluminum is added to remove dissolved oxygen in the steel. The quantity of inclusions is governed by the deoxidation process (1).

The steel is poured and allowed to solidify to form an ingot. The ingot is then hot rolled and cold rolled into the final form of the steel. During hot rolling the grains are elongated and may undergo preferred orientation. This rolling or working of the steel (strain hardening) increases its hardness and decreases its ductility. To remove the hardening, the material can be annealed. Annealing is a process whereby this steel is heated to approximately 1950 °F. After the annealing process, the material is cooled rapidly, often with water.

Microstructure of Type 347 Stainless Steel

The microstructure can be divided into three convenient categories: 1) non-metallic inclusions, 2) metallic inclusions, and 3) the matrix of the stainless steel. Non-metallic inclusions usually are divided into two types: endogenous and exogenous inclusions. Endogenous inclusions are formed from homogeneous reactions and usually consist of oxides and sulfides. Inclusions formed by mechanical entrainment or heterogeneous reactions are exogenous inclusions (2). Exogenous inclusions result mainly from contact between molten steel and ladle refractories. Exogenous inclusions are generally larger than endogenous inclusions and are usually irregular in shape and have a complex nature (3). Exogenous inclusions are found in steels in relatively low and unpredictable numbers.

Of the many types of endogenous inclusions, low carbon aluminum killed steel contains mainly two: manganese sulfide (MnS) and aluminum oxide (Al_2O_3) (1). MnS is formed while the ingot is cooling. In the hot liquid steel the sulfur is bonded with iron, forming FeS. When the steel cools the sulfur combines with manganese to form MnS (1). MnS has a lower free energy of formation than FeS as the steel cools. To insure all the FeS is transformed to MnS, the Mn:S ratio should be larger than four (4).

The only phase of MnS reported in steel is αMnS (4). This phase of MnS appears gray in a reflected light microscope (5). MnS has a melting temperature of 2930 °F and a microhardness of 170 kg/mm^2 (4). Chao has reported a value of 140 DPH (modified Vickers) (6). Austenite (γ) is harder than MnS at the lower end of the γ-range.

There are three types of MnS inclusions: Type I - globular, Type II - dendritic and Type III - irregular. In aluminum killed steel with a low oxygen content, Type II inclusions will form. Type II inclusions precipitate late in the solidification process - hence they are called dendritic. Type II inclusions usually form at grain boundaries. Often MnS solidifies around an Al_2O_3 nucleus (4). In chromium-nickel steels, MnS inclusions form at the cast austenite grain boundaries (7, 8). Chromium has been observed in MnS (7).

Let us next consider the effect of MnS inclusions on the steel. Due to the plasticity of MnS, the inclusions elongate along the rolling direction during the rolling process. This is one of the causes of the anisotropic nature of a plate of rolled steel. When the sulfur concentration is reduced to 0.005 percent (normally around 0.03 percent), the anisotropic nature of the plate still exists (2). Anisotropic behavior is affected by the sulfur content but is a function of other variables also (possibly preferred orientation of the grains).

After the deoxidizing process is complete, some aluminum remains in the molten or liquid steel in the form of Al_2O_3 (9). The only phase of Al_2O_3 observed in steel as inclusions is αAl_2O_3. The melting point of Al_2O_3 is 3722 °F. The microhardness is 3000-4500 kg/mm^2 (9). Sims suggests that oxide inclusions, due to their higher hardness and higher modulus of elasticity, cause higher local stresses than a softer sulfide inclusion (2). He also states that sulfides have a better bond to the matrix than do oxides. Tenembaum has observed no Al_2O_3 inclusions larger than 30μm, suggesting that larger inclusions may have been broken up in the rolling process.

The presence of metallic inclusions is determined by the chemical composition, the mechanical working and the heat treatment of the steel. The potential types of second phase particles present in Type 347ss are delta ferrite, sigma, and carbide particles.

Delta ferrite is formed in the liquid steel. As the steel solidifies, the amount of delta ferrite decreases. The presence of "delta" indicates that the ferrite has been formed at high temperatures (10). The chemical composition of the steel is the primary factor in determining the amount of ferrite (11). Heat treatment can increase or decrease the amount of ferrite in the steel. The ferrite is reported to contain more chromium than the matrix (11) and less carbon

(12). As the ferrite grows, a build up of carbon may develop around the ferrite particles (12). The ferrite phase appears in the light microscope as a separate and well defined phase in the austenite. Below, 1100 °F., delta ferrite will have little effect on Type 347ss after fabrication. This phase may cause some problems during hot working conditions (10).

The sigma phase is harder to form and is more detrimental than the delta ferrite phase. This hard and brittle phase will form in Type 347ss when the steel is subjected to a temperature range from 1000 to 1700 °F. The quickest way to form the sigma phase is to convert the ferrite to sigma. Between 1000 and 1700 °F., this conversion can take place in a matter of hours. An anneal and water quench should remove all the sigma phase (10, 11). This phase will lower ductility and may affect corrosion resistance.

Niobium (Nb) and tantalum are added to Type 347ss to combine with the carbon and precipitate in the steel between and inside grains as niobium carbide (NbC) and tantalum carbide (TaC). If the carbides are uniformly distributed intragranularly, they will increase the strength. To hold the carbides in solution, Type 347ss is annealed to some temperature below 2000 °F and rapidly cooled. Once carbides precipitate, they are rather difficult to get into solution.

Fracture

There are four basic mechanisms of fracture: plastic deformation, cleavage, creep and fatigue. Since stainless steel fracture occurs primarily by the mechanism of plastic deformation, only this method will be discussed.

In the past, fracture has been described in terms of its macroscopic fracture characteristics: mode, behavior and appearance. Mode indicates the path of the fracture surface through the material. Behavior indicates the amount of plastic deformation that occurs before fracture occurs. Appearance traditionally has referred to macroscopic appearance, but the transmission electron microscope (TEM) and scanning electron microscope (SEM) have permitted researchers to observe fracture surfaces with greater magnification and depth of field (13). The SEM and TEM have been compared by several researchers, for example, Russ (14), Johari (15), and Pelloux (16). The SEM has been shown to be an excellent new tool for studying fracture surfaces.

In the plastic fracture mechanism, fracture occurs after considerable plastic deformation of the specimen sample. Plastic deformation fracture has not been studied in the past with as much emphasis as the other mechanisms of fracture. The reason for this is that plastic deformation failure can be avoided by proper design whereas this is not the case with the other fracture mechanisms.

Plastic fracture is also called rupture, dimple fracture or ductile fracture. Some of these terms are misleading. For example, rupture means deformation with 100% reduction in area. This might be considered a limit of ductile fracture. Plastic fracture can be described more precisely in terms of the three macroscopic properties mentioned above. The mode of plastic fracture (or path taken by a crack or fracture surface) is transgranular but can be intergranular. In reference to the behavior characteristic, plastic fracture is usually ductile. A typical macroscopic appearance of tensile fracture is the cup-and-cone appearance.

Microscopic Aspects of Plastic Fracture

The first stage of plastic fracture is microvoid formation. The second stage is microvoid growth and coalescence. The third stage is final separation (13).

There are two theories on microvoid formation. The theory generally considered is that particles or inclusions in the matrix cause the void formation, as first suggested by Tipper (17). The other theory is that voids form without particles or inclusions present.

The theory that particles or inclusions form voids has much supporting work. There are two ways that voids can form from particles. If the particle is brittle, it may break. Due to tensile load the two fragments can separate

thus forming a void. Gurland and Liu (18) have displayed reflected light photographs of carbide particles forming voids in this manner. The carbides were located in 0.30% carbon steel under tensile load. Baker and Smith (19) have suggested that inclusions are broken during rolling and a plane of weakness exists between the particles. Their study concerned oxide inclusions in a copper matrix. In addition to the possibility of particle fracture, decohesion of the particle-matrix interface may occur. Spretnak (20) suggests that the interface bond being broken in tension is not an accurate description of the process. He suggests, rather, that the mechanism of decohesion arises from the hydrodynamic nature of the matrix when dislocation density increases with plastic flow.

The second theory is supported by Rogers' work with oxygen-free, high-conductivity copper (21). He suggested that voids form to reduce the stresses in local regions, where deformation is particularly intense. It is important to stress that his instrument resolution capabilities to detect the presence of particles was limited to particles approximately 2μm in diameter. Rogers observed void formation at grain boundaries. After extensive necking had occurred, some voids were nucleated within grains. He suggests that "voids are formed to relieve the high stress created at local regions where the inhomogeneous deformation is particularly

intense" (21, p. 501). Rogers proposed a "void sheet mechanism. Void formation occurred catastrophically within this heavily deformed zone and failure of this sheet of voids separated the specimen" (21, p. 503).

After microvoid formation occurs, the next stage of plastic fracture is void coalescence. Voids grow together by internal necking (13). The walls between voids thin down and separate by rupturing; this is called coalescence. When enough voids coalesce, the area can be called a crack, forming the initiation of the third stage of plastic fracture. This crack can propagate by void formation on its own.

EXPERIMENTAL METHOD

Sample Preparation

Samples were cut from a plate of Type 347ss. The plate thickness was 0.198 $\pm$ 0.003 inch. It is assumed that the plate was hot rolled and then cold rolled. The samples were to be tensile tested so they were formed into bars. The bars were first rough cut from the plate with a friction saw to a size of 1/2 inch by 8 inches. Samples were then machined to a width of 0.401 $\pm$ 0.001 inch. The samples were prepared with the bar axis both parallel to the rolling direction of the plate and parallel to the transverse direction of the plate (Figure 1).

All bars were annealed at 1950 °F for twenty to thirty minutes and then were water cooled. This gave all bars a common heat treatment and relieved stresses from cold rolling, friction cutting or machining. The hardness was measured before and after annealing. A Rockwell hardness tester was used with a 1/16 inch ball indenter and a 100 kg load. The average hardness before and after annealing was 85.1 and 78.5, respectively, on the Rockwell B scale.

A Soutewark-Emery Universal Testing Machine (capacity of 60,000 pounds) was used to deform and fracture the samples. The ultimate load and fracture load of the steel were obtained from this machine. After fracture occurred, the cross sectional areas of the bars were measured at the fracture

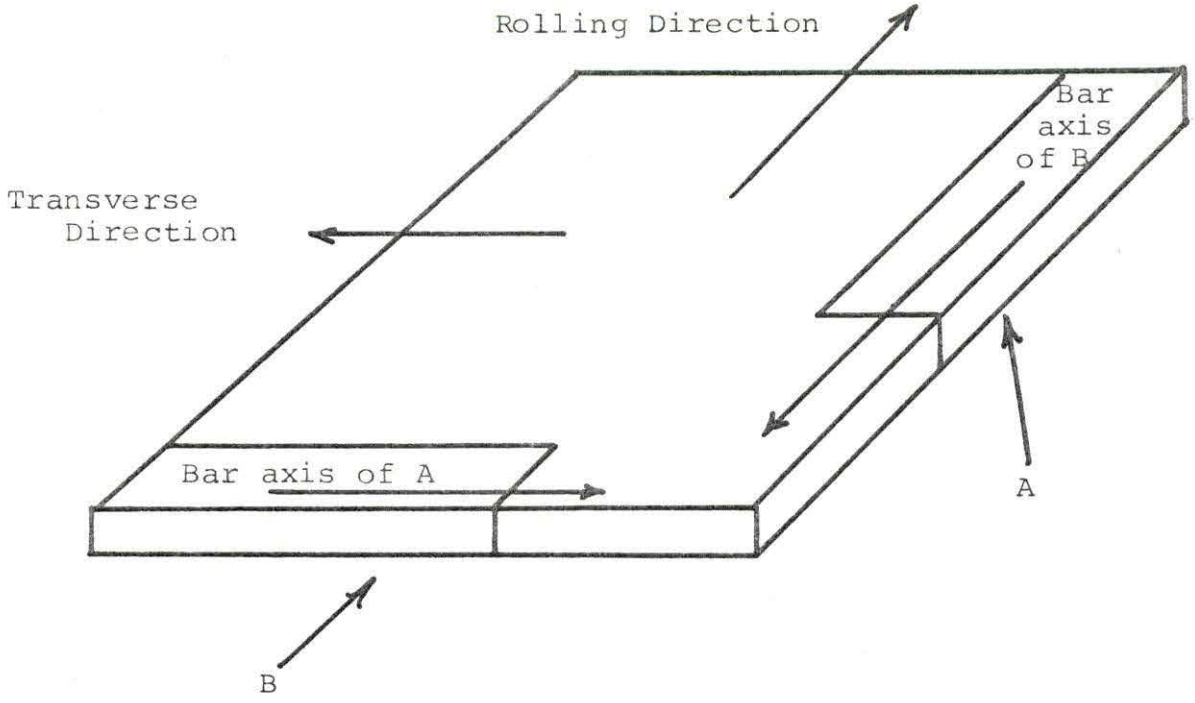

Figure 1. Two types of samples were cut from a plate of stainless steel. Sample Type A was cut with its bar axis parallel to the rolling direction. Sample Type B was cut with its bar axis perpendicular to the rolling direction

surface to obtain reduction in area data.

Polished samples were required for both the reflected light microscope and the microprobe. Polishing was done with silicon carbide, 100 to 600 mesh grit size. Final polishing was done with either Al_2O_3 or diamond paste. Final polishing on the deformed samples utilized a vibratory polish with Al_2O_3.

Studying the Microstructure

Samples were observed using a reflected light microscope. This instrument can be used to obtain relatively fast, inexpensive and qualitative information. MnS inclusions can be identified by their gray color and transparent nature. Reflected light microscopy was used primarily for preliminary surface observations. Absolute chemical identification of inclusions was not possible with this instrument.

Since chemical information was required for study of the inclusions (these inclusions were approximately 10μm in size), a microprobe x-ray analyzer was utilized. Two microprobes were used: an Hitachi Electron Probe Microanalyzer, Model XMA-5, and an Applied Research Laboratories EMX model.

A microprobe analyzer uses an electron gun to supply an electron beam. The electrons are accelerated and focused before they strike the target. When the beam strikes the target, the electrons are elastically scattered (with no energy loss) through an angle of approximately 180 degrees;

these are called reflected electrons. The beam of electrons may interact with electrons bound to the target atoms. Some of these bound electrons may be knocked out of the surface; these are known as secondary electrons. As the electrons interact with a target atom, they may excite the atom. When the atom resumes its ground state, an x-ray is given off. The important thing about the emitted x-ray is that it is unique for each element; therefore, each element has its own characteristic x-ray. In order to determine the atomic number of a specific target atom, it is necessary to find the energy of the x-ray. A curved crystal is used to disperse the x-rays. This crystal will separate x-rays of different energies so they may be analyzed according to their energy levels. Another type of information the microprobe can supply is that of absorbed electrons or specimen current. The specimen current is approximately equal to the beam current minus the reflected electron current. The specimen current information is similar to that obtained from reflected electrons.

In using a microprobe, x-ray emission is the principal concern. There are several modes of operation of a microprobe. One of these is the quantitative method. In this case, the beam is focused on one area of the specimen and the x-rays are counted for the elements present. These counts are compared with the counts from a standard sample. The standard

sample contains a known amount of a certain element of interest. The counts obtained from the sample and standard are analyzed by a computer which determines the composition of the sample. The computer is programmed to correct for drift, wavelength shift, dead time, and atomic weight. The computer also corrects for x-ray interactions. For example, the x-rays from type A atom may be absorbed to some extent by type B atom. The B atoms would then give off x-rays characteristic of B atoms. This interaction would give a false reading for both A and B. The intensity of A's x-ray would be too low and that for B would be too large. These phenomena are called absorption and enhancement, and are corrected for in the computer program.

When an evaluation of the change in composition of the sample is required, the scanning mode of a microprobe can be used. In this case, the beam can be scanned across the sample providing a single line profile or a number of these lines to build up a two dimensional or three dimensional elemental display. Changes in the x-ray count will denote change in composition in reference to any one element. This technique is very useful when working with inclusions.

Reflected electrons can supply chemical and limited topographical information. The intensity of reflected electrons is closely related to the atomic number of the atoms present. Therefore, a relative idea of chemical composition

can be obtained. Absorbed electrons supply similar information.

A conventional microprobe can have a secondary electron detector system which can be used for obtaining topographical information. The secondary electron system on the Hitachi microprobe was found to be very unsatisfactory because of poor resolution. Very little detail could be obtained from the secondary electrons.

In this study, an attempt was made to identify inclusions or particles on the fracture surface. The surface was found to be too rough for purposes of using a conventional microprobe to identify these particles on the surface. Satisfactory results were not obtained, the major problem being orientation and location on the fracture surface. The optical microscope was no help in finding identification marks on the fracture surface because of its low depth of field. Another method of inclusion identification on the fracture surface was necessary. Topographical and chemical information of the fracture surface was needed. Topographical information could be obtained, however, by either the TEM or the SEM.

Much work had been done with the TEM on fracture surfaces before the SEM became available. The TEM has a major shortcoming, as compared to the SEM, for studies of fracture surfaces. Fracture surfaces can exhibit too high a degree of surface relief to permit direct study with the TEM. Instead,

a direct technique using a one, two, or three-step replica must be employed. The preparation of replicas is very time consuming and requires great skill. If a surface is rough, it will be difficult, and in some cases, not possible to replicate. Holes in the surface will tend to produce artifacts when the replica is removed from the fracture surface, complicating interpretation capabilities.

By comparison, SEM results can be interpreted directly, because the fracture surface itself is examined instead of a replica. SEM requires little or no sample preparation, has a large depth of field, has a resolution approaching 100 Å, large areas of the sample may be studied, and samples may be studied for a number of orientations (15). Because of these advantages and because of the TEM shortcoming, an SEM was used to obtain the topographical information of the fracture surfaces. A Cambridge Stereoscan SEM, Model II A, was used to obtain all SEM micrographs in this work.

Chemical information also can be obtained from the SEM. When the SEM electron beam strikes the sample, x-rays are generated, as in the case of the microprobe. A conventional SEM can be adapted with an energy-dispersive or a wavelength-dispersive system to count and measure the energy of the emitted x-rays.

The wavelength-dispersive system is very similar to the system used on the microprobe. Curves crystals are used

to disperse the x-rays so they may be counted by a gas flow proportional counter. A Cambridge SEM, Model S4, with a wavelength-dispersive system was used in a preliminary investigation. This instrument was not available for additional studies at that time. Only three of these complete systems are currently in operation in the United States.

However, energy-dispersive systems are more widely available and have proven to be very useful in chemical characterization of samples. The energy-dispersive system counts the x-rays with a semiconductor detector. The energy of the x-ray is measured using a multichannel pulse height analyzer. This analyzer, in connection with a teletype printer, typically outputs 400 intensities. Each intensity x-ray corresponds to a discrete energy range. This type of system was used to study the chemistry of inclusions present on the fracture surfaces. The energy-dispersive system used for the investigations consisted of a Princeton Gamma-Tech X-ray Spectrometer used on a JEOLCO SEM, Model JSM-2. The measured resolving capability of this system was 330 eV for 6.4 keV Fe K_{α} radiation.

One problem with the microprobe and SEM is that of spatial resolution of features when using x-rays. The beam of the microprobe is approximately 2μm in diameter while the SEM beam is significantly smaller, tens of Å. The problem comes from the fact that x-rays are not generated at the

surface of the sample, but come from a volume beneath the surface. For the microprobe, the diameter of this volume is approximately 4 to 6μm. Thus, 1 micron diameter particles may be difficult to detect and to identify. Another problem is that the electron beam may pass through thin inclusions of 1 to 5μm and generate matrix chemical information and thus complicate interpretation of inclusion chemical information.

RESULTS AND DISCUSSION

This investigation emphasizes results from three areas: tensile tests, microprobe analysis, and SEM analysis. The tensile tests show that the rolling direction was stronger than the transverse direction. Twelve bars were tensile tested, six parallel to the rolling direction and six parallel to the transverse direction. The average ultimate stress of the rolling and transverse directions were $87.3 \pm 1.14 \times 10^3$ psi and $84.7 \pm 0.80 \times 10^3$ psi, respectively. The rolling direction was a small, but significant, amount stronger than the transverse. There was no significant difference in reduction of area between samples parallel to the rolling direction and those parallel to the transverse direction. The fracture surfaces were cut from the fractured bars for SEM investigation (Figure 2).

Before studying the fracture surfaces, two areas were investigated: the undeformed samples and the partially deformed (but not fractured) samples. Studies of the original state of the material and the state of partially deformed material were performed to help understand the mechanism of fracture of the material.

The undeformed samples were studied with a reflected light microscope and the microprobe analyzer. Two types of inclusions were anticipated to be present in the steel: MnS and Al_2O_3. In addition, NbC was identified. The final

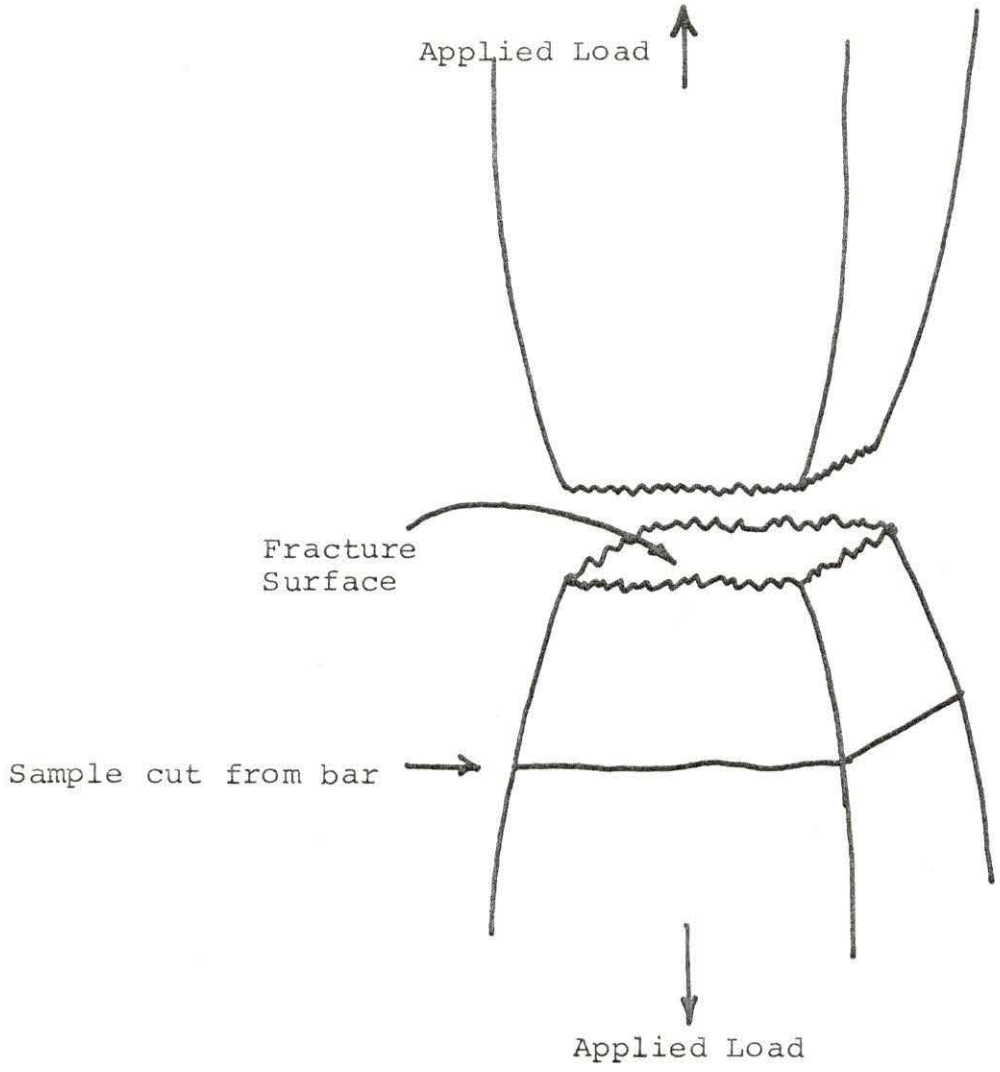

Figure 2. After samples have fractured, the fracture surface is cut from the remaining part. The vertical direction is parallel to bar axis and the direction of applied load

polishing compound used was Al_2O_3 (0.34μm particle size). To identify Al_2O_3 inclusions, a sample was polished with silicon carbide and diamond paste. Al_2O_3 inclusions were difficult to locate but were found and identified. Additional samples were polished with silicon carbide and Al_2O_3.

Typically, MnS inclusions were elongated and found in the vicinity of other elongated inclusions. These varied from 3 to 5μm in length and from 1 to 2μm in diameter. All inclusions or groups of inclusions were elongated in one direction. Evidence was developed that the particles are flattened slightly during rolling as well as elongated.

A large number of NbC particles was located on the fracture surface as compared with the Al_2O_3 and MnS. Results of the literature survey suggested that NbC particles would be very small particles. Linnert (10) published reflected light micrographs of NbC particles in Type 347ss of two types of distributions, fine dispersed particles indicating proper heat treatment and massive particles formed during improper treatment. The NbC particles observed in this research were found to be dispersed and of a size range in agreement with the steel having received proper heat treatment.

The NbC particles were generally found in groups or clusters. The clusters, not the particles themselves, were elongated in the same direction as the MnS inclusions. MnS particles are ductile at rolling temperatures while NbC

particles are brittle; therefore, the NbC particles are not deformed but can be fragmented. The size of the NbC particles on the average was larger than the MnS particles. The size range for NbC particles was approximately 1μm to 50μm. The dispersion of particle size was much larger in the NbC particles as compared with the MnS particles. NbC particles were relatively more abundant than MnS particles.

Samples that were partially deformed were studied by the optical microscope and by the microprobe analyzer. From the optical microscope, fractured particles were observed (Figure 3). It is important to consider when these particles were broken. They could have been broken during the rolling process (which broke up larger particles) or they could have been broken during the tensile testing. The second theory is more probable. If the particles were broken up during rolling, it is likely that they would have been pulled apart. In the rolling process, the material was deformed on a large scale in reference to the NbC inclusions. Any cracked or fractured particles would be pulled apart by the large amount of material flow associated with rolling. Therefore any particle fractured during rolling would appear in the matrix as a separate unfractured particle. The fractures observed in Figure 3 must be the result of tensile testing.

Often these NbC particles are broken several times, the fracture planes being parallel to one another. The smaller

Figure 3. The reflected light micrograph represents a polished surface of a partially deformed sample. The bar axis and rolling direction are parallel the shorter edge of the micrograph. The lighter colored particles have been fractured during tensile testing. The dark areas between particles are voids. The length of the scale bar represents 10μm

NbC particles (approximately 1μm in size) have not initiated voids. Generally they appear intact and completely surrounded by the matrix. There is evidence in some cases that the matrix-particle interface has been broken around the larger inclusion.

Gray particles were also observed in the reflected light microscope and identified as MnS by the microprobe analyzer. These particles were also observed to form voids by inclusion fracture and surface separation. Due to the smaller number of MnS particles, they initiated fewer voids than NbC particles.

After undeformed and partially deformed samples were studied, the fracture surfaces were studied with microprobe and SEM to obtain topographical and chemical information. Topographical information was used to describe the mechanisms of fracture. Chemical information would identify possible inclusions on the fracture surface.

The microprobe was first used to study the fracture surfaces. The microprobe is an excellent instrument for studying inhomogeneities 5μm and larger on polished (flat) surfaces. On a fracture surface, particle size typically varies from 0.5μm to 10μm. As stated earlier, the surface was too rough for the purpose of accurately using a conventional microprobe to identify these particles on this surface. Identification of these particles was attempted but was not

accomplished satisfactorily.

A preliminary investigation of a fracture surface with a wavelength dispersive system was made. Satisfactory results were obtained, but the system was not available for further research as described earlier.

However, an energy dispersive system was available and was used to obtain data in this investigation. Data for the matrix and four inclusions were obtained from the energy dispersive system. A complete tabulation of this data is given in the Appendix. Data for a selected energy region of direct interest for each inclusion and the matrix are given in Figures 4, 5, 6, 7 and 8. SEM micrographs of these four inclusions are shown in Figures 9a, 9b, 10a and 10b.

In comparing Figures 4, 5, 6, 7 and 8, differences in intensities are apparent. The intensity of the x-rays will be affected by the geometry of the areas around the inclusion. The geometry of the particles may also affect the intensity. The size of the particle will also affect the intensity of matrix background counts. When the beam is focused on an inclusion, there is a possibility that the volume of excited material will overlap into the matrix. Therefore the size of the inclusion will affect the amount of matrix material excited.

The chemical analysis for the matrix (Figure 4 and Table 1, Appendix) shows definite evidence of Cr, Fe, and Nb, and the

Figure 4. A plot of x-ray energy versus x-ray intensity for the matrix is shown. A 25 keV electron beam was used to excite the x-rays, and absorbed specimen beam currents were 9×10^{-11} amperes. Complete data is tabulated in Appendix Table 1

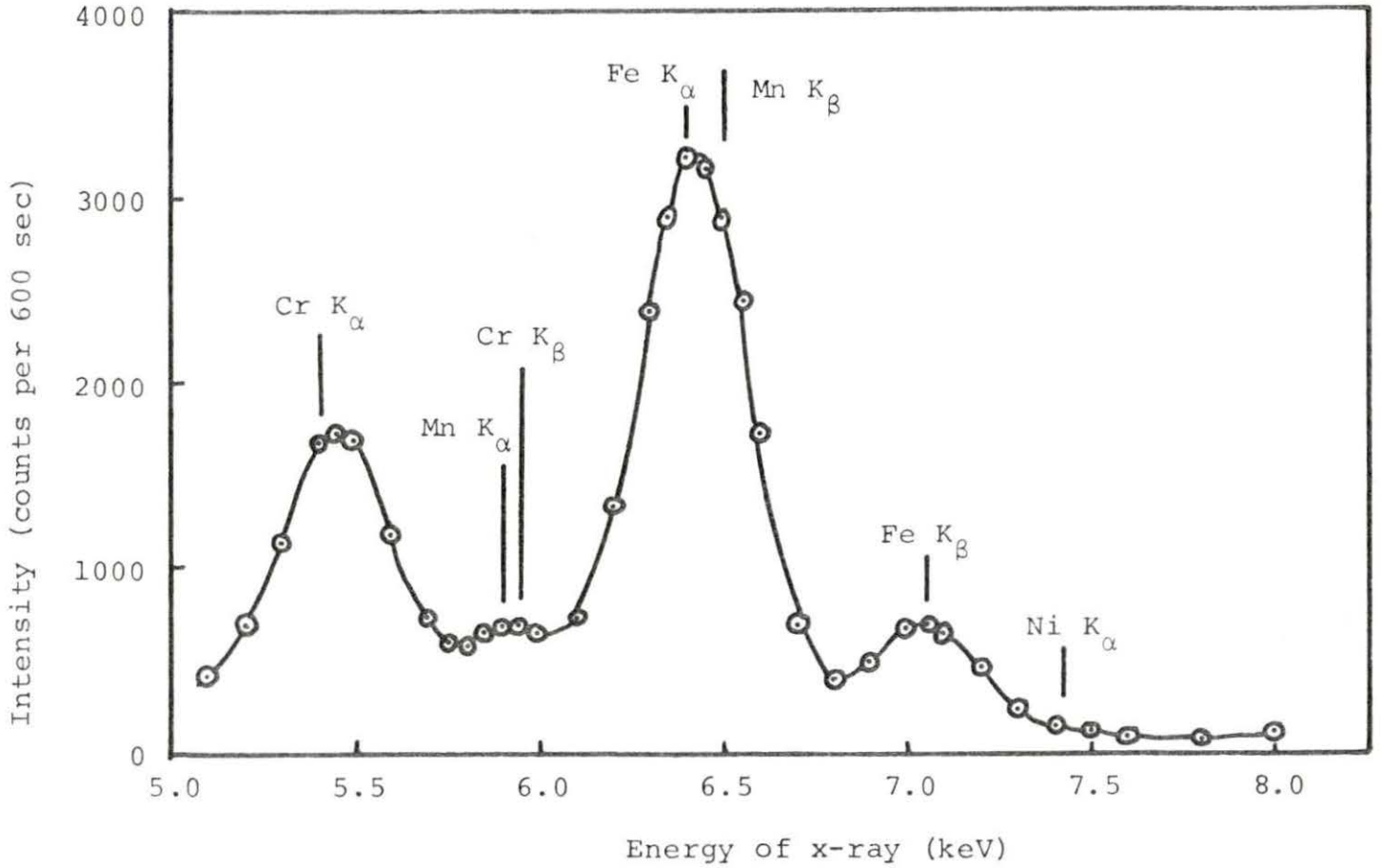
4000
3000
2000
1000
0
Intensity (counts per 600 sec)
Cr K_α
Cr K_β
Mn K_α
Fe K_α
Mn K_β
Fe K_β
Ni K_α
5.0
5.5
6.0
6.5
7.0
7.5
8.0
Energy of x-ray (keV)

Figure 5. A plot of x-ray energy versus x-ray intensity for an inclusion (number 1 in Figure 11, also Figure 9a). A 25 keV electron beam was used to excite the x-rays. For complete data see Appendix Table 2

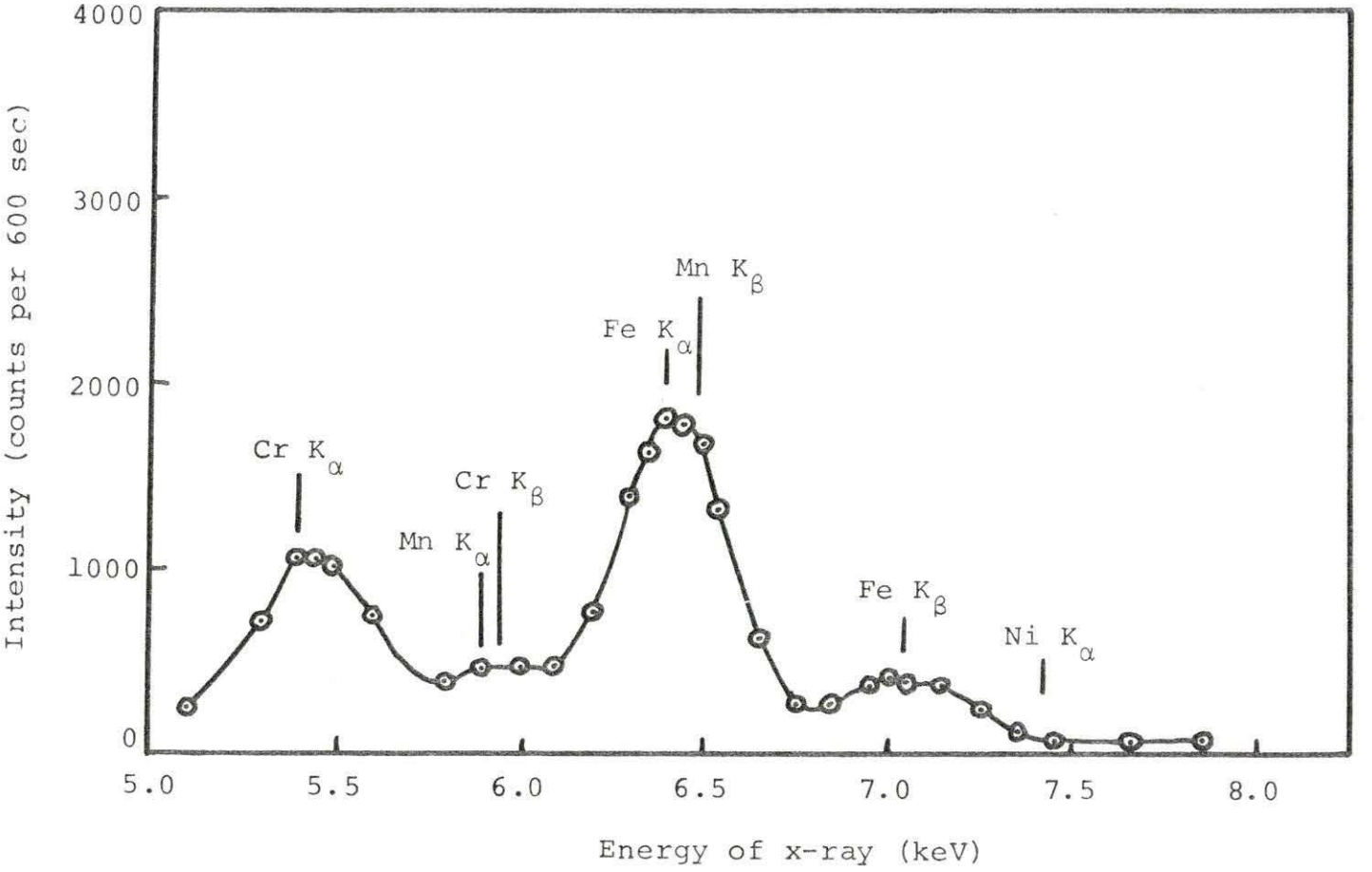
4000
3000
2000
1000
0
Intensity (counts per 600 sec)
Cr K_α
Cr K_β
Mn K_α
Fe K_α
Mn K_β
Fe K_β
Ni K_α
5.0
5.5
6.0
6.5
7.0
7.5
8.0
Energy of x-ray (keV)

Figure 6. A plot of x-ray energy versus x-ray intensity for an inclusion. A 25 keV electron beam was used to excite the x-rays. For complete data see Appendix Table 3

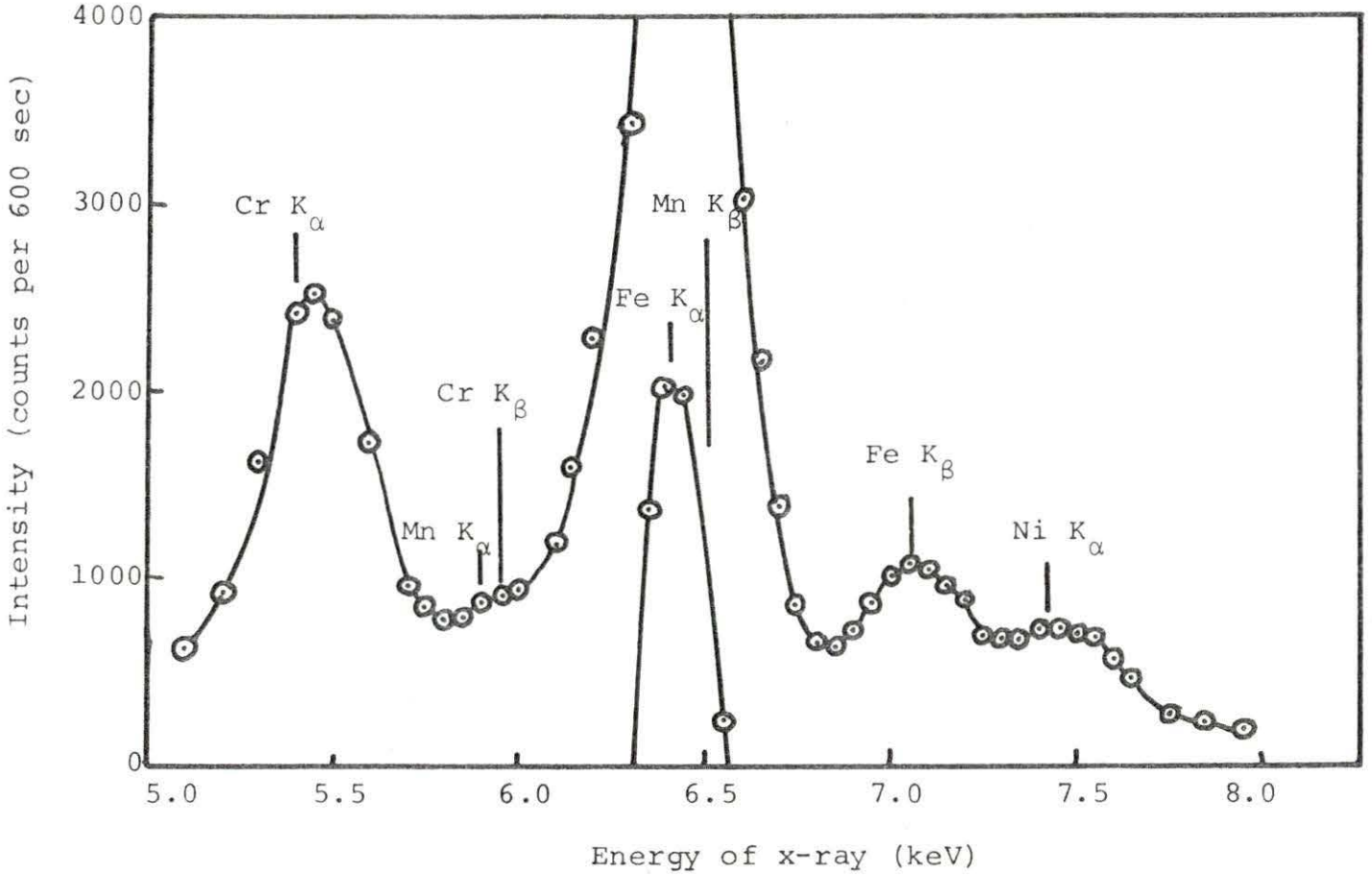
Intensity (counts per 600 sec)
4000
3000
2000
1000
0
Cr K_α
Mn K_α
Cr K_β
Fe K_α
Mn K_β
Fe K_β
Ni K_α
5.0
5.5
6.0
6.5
7.0
7.5
8.0
Energy of x-ray (keV)

Figure 7. A plot of x-ray energy versus x-ray intensity for an inclusion (number 2 in Figure 11, also Figure 10a). A 25 keV electron beam was used to excite the x-rays. For complete data see Appendix Table 4

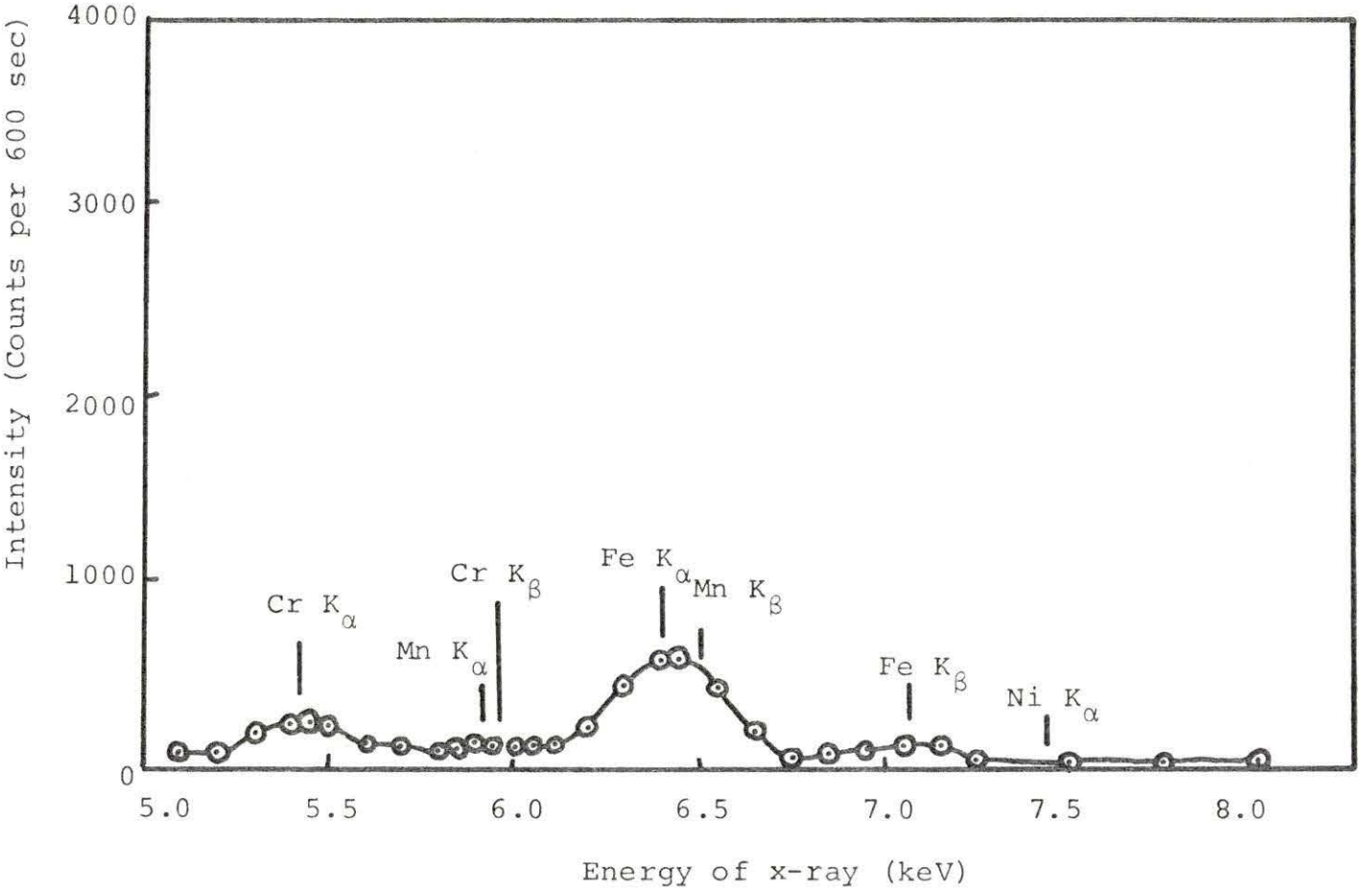
Intensity (Counts per 600 sec)
4000
3000
2000
1000
0
Cr K_α
Mn K_α
Cr K_β
Fe K_α
Mn K_β
Fe K_β
Ni K_α
5.0
5.5
6.0
6.5
7.0
7.5
8.0
Energy of x-ray (keV)

Figure 8. A plot of x-ray energy versus x-ray intensity for an inclusion (number 3 in Figure 11, also Figure 10b). A 25 keV electron beam was used to excite the x-rays. For complete data see Appendix Table 5

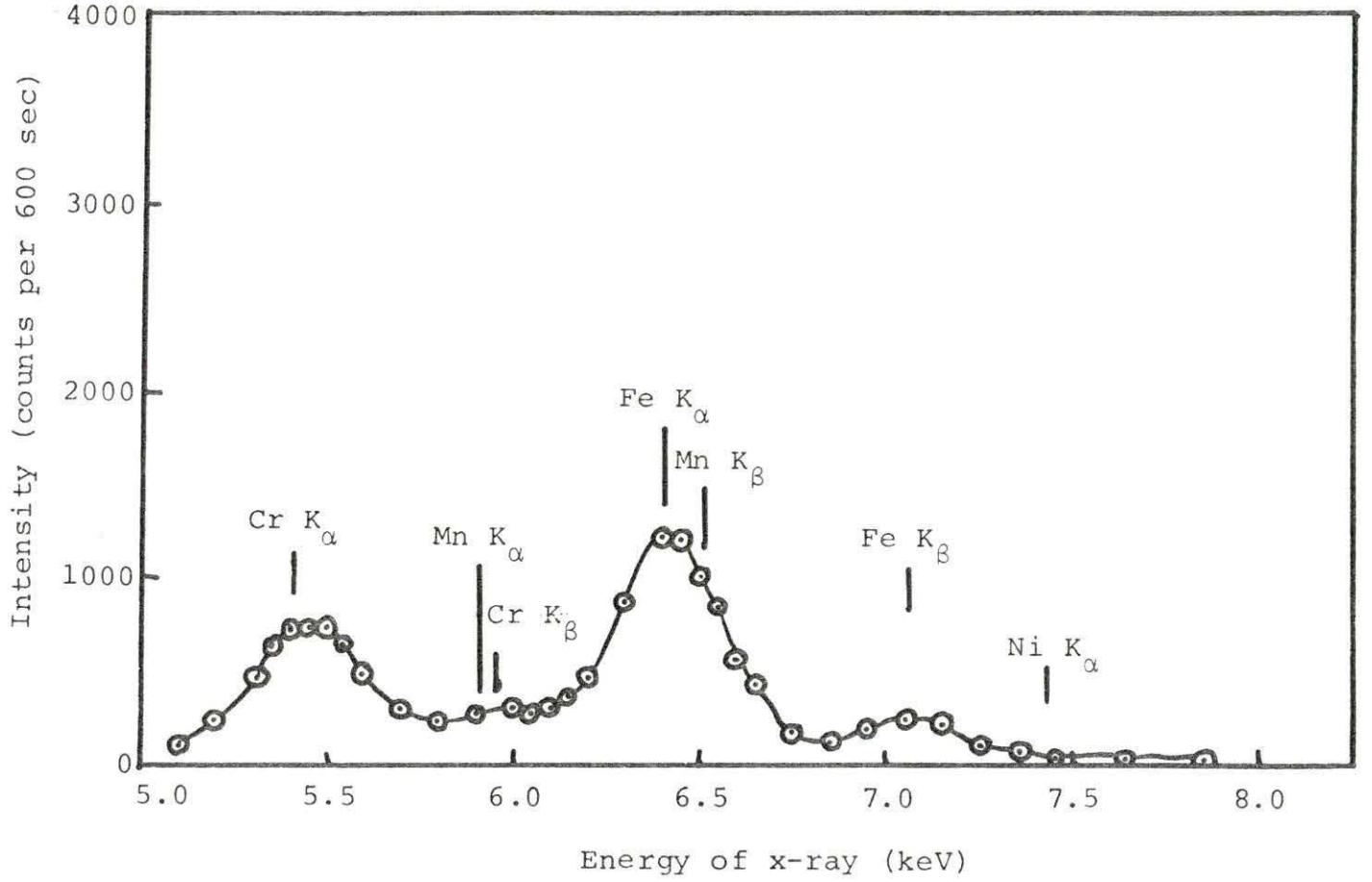
4000
3000
2000
1000
0
Intensity (counts per 600 sec)
Cr K_α
Mn K_α
Cr K_β
Fe K_α
Mn K_β
Fe K_β
Ni K_α
5.0
5.5
6.0
6.5
7.0
7.5
8.0
Energy of x-ray (keV)

Figure 9a. The SEM micrograph shows a dimple on a fracture surface with a fractured inclusion at the bottom of it. This area is located on Figure 11 by arrow 1. The rolling direction is parallel to the horizontal edge of the micrograph. The length of the scale bar represents 2μm

Figure 9b. The SEM micrograph shows a dimple with an inclusion located inside the dimple, on a fracture surface. Note the tear features associated with the dimples approximately 0.4 μm in diameter. The rolling direction is perpendicular to the plane of the micrograph. The length of the scale bar represents 5μm

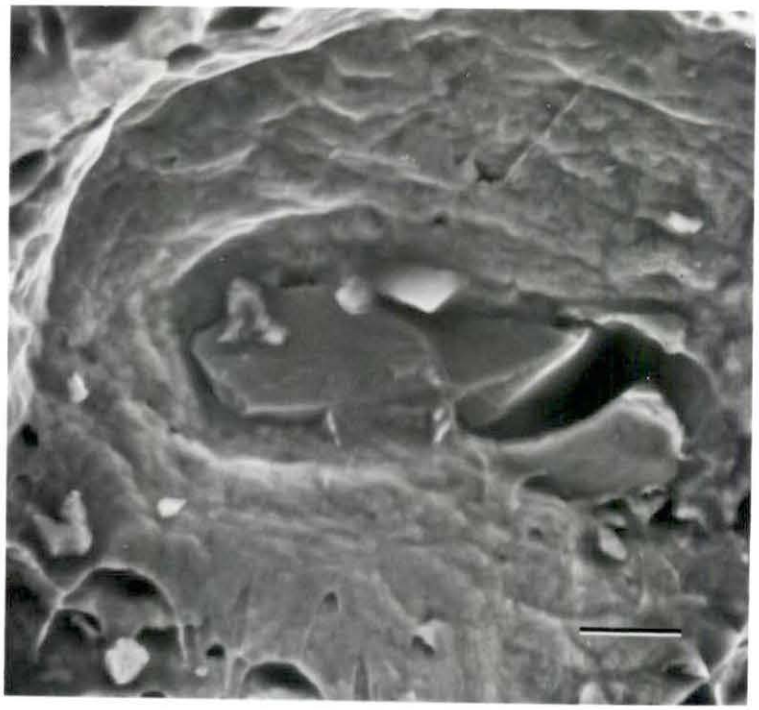

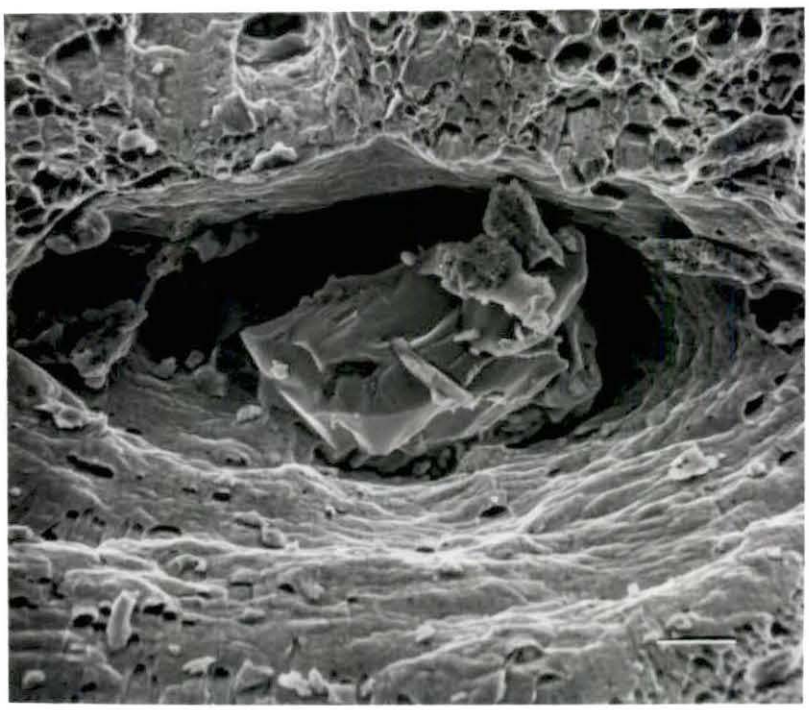

Figure 10a. This SEM micrograph shows several dimples and associated inclusions on a fracture surface. This area is located in Figure 11 by arrow 2. The rolling direction is parallel to the horizontal edge of the micrograph. The length of the scale bar represents 1μm

Figure 10b. The SEM micrograph shows an inclusion on the fracture surface. This area is located in Figure 11 by arrow number 3. The rolling direction is parallel to the horizontal edge of the micrograph. The length of the scale bar represents 1μm

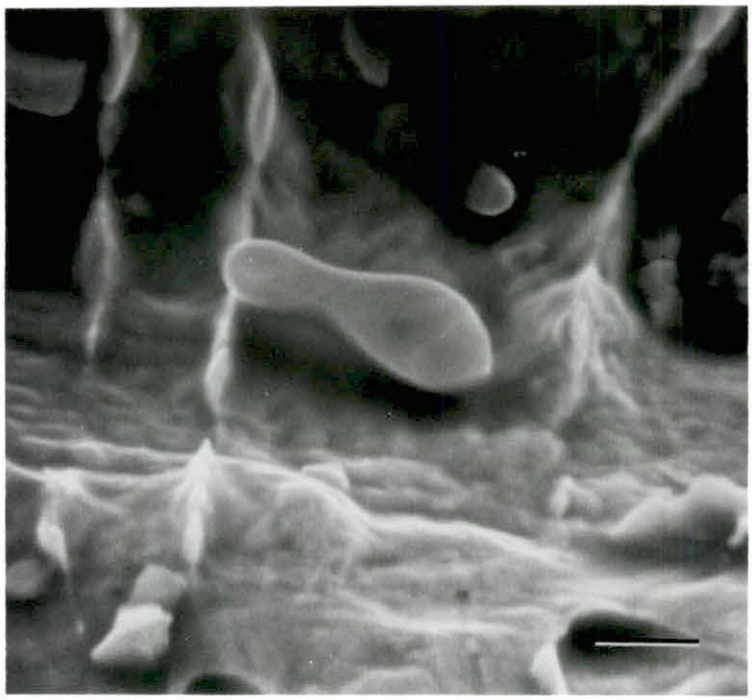

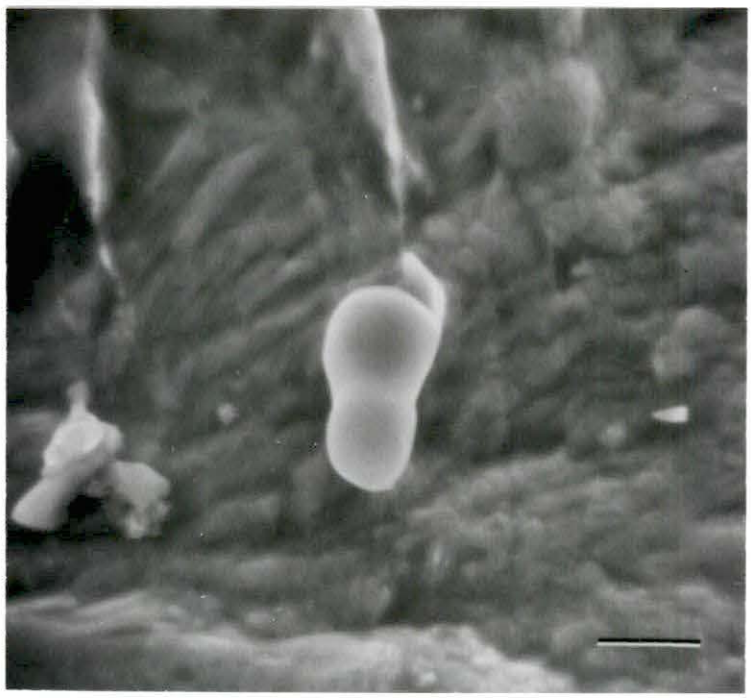

Mn K_α and Cr K_β lines. For each peak the shape of the curve associated with it was assumed to be a normal distribution. Knowing the peak value, full width at half maximum, and the energy of the peak, the shape of the curves could be plotted. Fe K_α, Cr K_α and Cr K_β curves were then added together and compared with Figure 2. The results of this attempt were unsatisfactory. Even though the results were not satisfactory, it is suspected that Mn is present in the matrix.

Figures 5, 6, 7, and 8 are very similar in shape to Figure 4; all show evidence of Cr and Fe. Again Mn is suspected to be present. No Nb peak was observed in the data for 5, 6, 7 and 8. The curves are similar except for Figure 6. Ni is also observed in Figure 6. The intensities of the peaks in Figure 6 are approximately double the intensity in figure 2. From this it is suspected that Ni was not observed in other areas because of lower counting rate and the Ni peak was not observable over background. A critical question here is how much is the excited volume of the electron beam is overlapping into the matrix.

Russ and Kabaya (22) examined 0.4 μm particles in a stainless steel matrix with a system similar to the one used in this investigation. They used an energy dispersive system on a JEOLCO JSM-2. The resolving power of the system was 380 eV. By comparison, the system used in this investigation for chemical analysis was also a JEOLCO JSM-2 with energy

dispersive system with a resolving power of 330eV for 6.4 keV radiation, which represents a better system than that used by Russ and Kabaya. However, a comparison of their results with those presented here point to the complexity of attempting this type of analysis.

A schematic of Russ and Kabaya's results is shown in Figure 12. In the stainless steel matrix they found Mn, Cr, Ni, and Fe. On the particle they found only Fe and Cr. This disappearance of the Ni and Mn peaks demonstrates that the volume of matrix excited was not very large. Comparing their data to the data developed in this investigation resulted in little correlation. Both sample materials are austenitic stainless steel. Minor components of Russ' and Kabaya's stainless steel and the steel used in this investigation may vary, but the major components should be similar. Therefore, the chemical displays for the matrix of Russ and Kabaya should be similar. However, they are not.

For samples of this investigation, no inclusions were found with Fe and Cr using microprobe analysis on deformed and undeformed surfaces. It is concluded that the matrix is being excited and most of the x-ray signal is due to the matrix. Russ and Kabaya have observed the opposite. They have observed a larger Mn peak than observed in this investigation. They have also observed an Ni peak in the matrix which was not found in this investigation. Some of these

Figure 11. This SEM micrograph identifies the location of three previously mentioned micrographs. Number 1 on this micrograph corresponds to Figure 9a, number 2 corresponds to 10a and number 3 corresponds to 10b. The rolling direction is parallel to the long side of the micrograph. The length of the scale bar represents 20μm

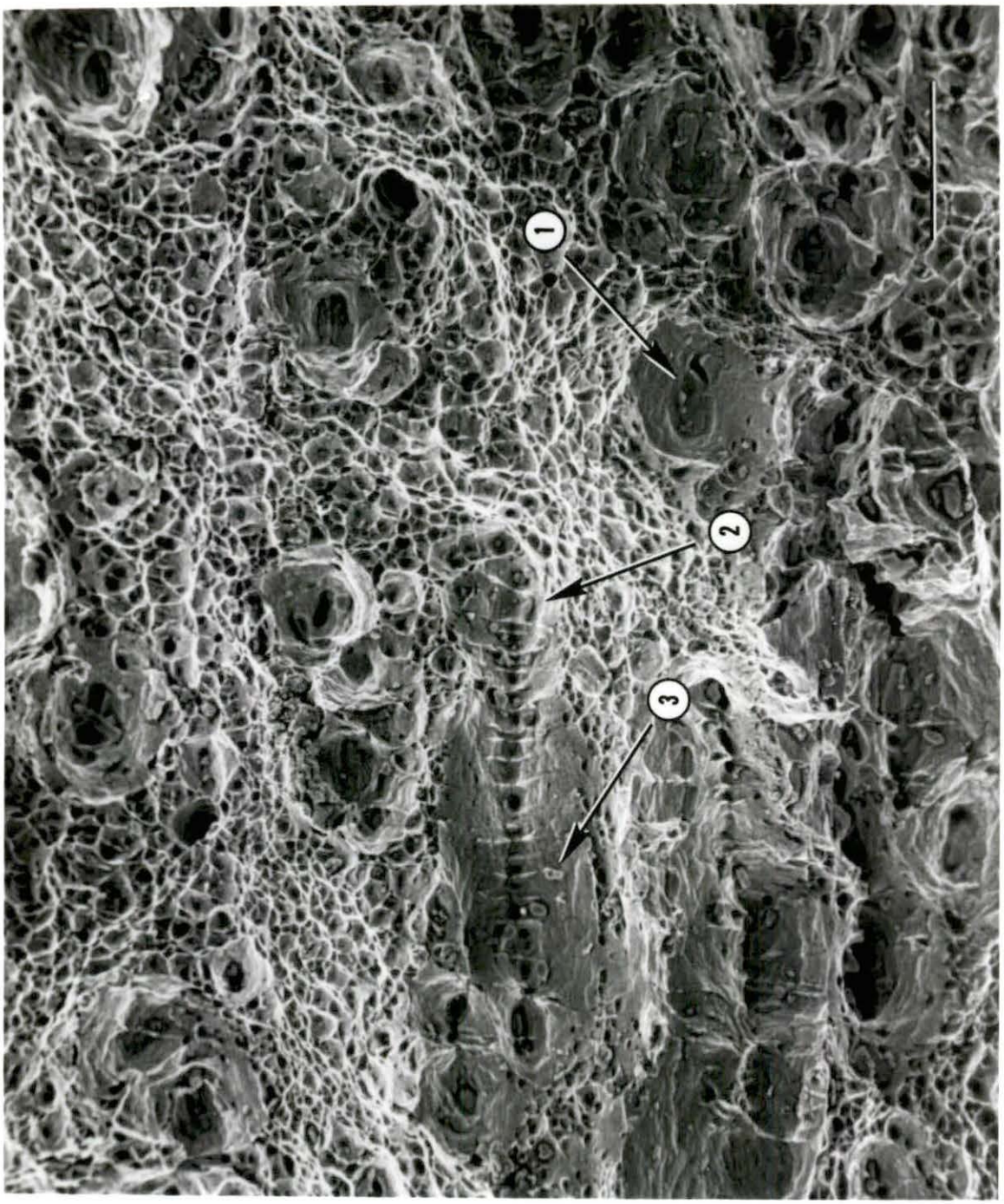
1
2
3

Figure 12a. X-ray intensity versus x-ray energy for a stainless steel matrix, after Russ and Kabaya (22, p. 63). Notice the presence of the Cr K_α, Mn K_α, Fe K_α and Ni K_α peaks. For their investigations 1000 second counting periods were used, with an absorbed specimen current of 6×10^{-12} amperes and 25 keV accelerating voltage

Figure 12b. X-ray intensity versus x-ray energy for a particle in a stainless steel matrix, after Russ and Kabaya (22, p. 63). Notice the absence of the Ni K_α peak when compared with the data from the matrix which appears in Figure 12a

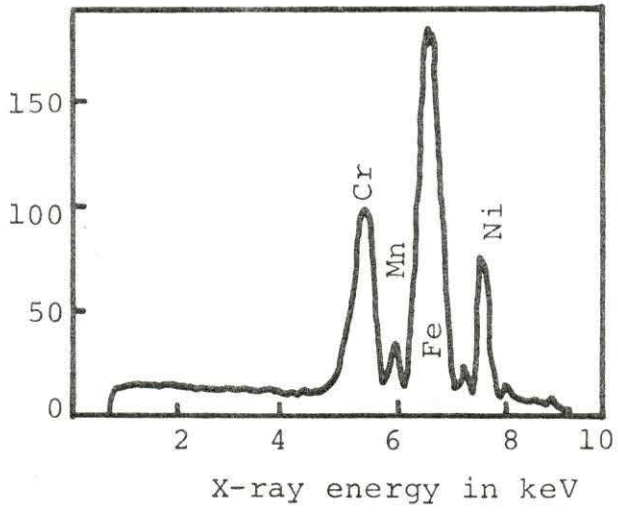
150
100
50
0
Cr
Mn
Fe
Ni
2
4
6
8
10
X-ray energy in keV

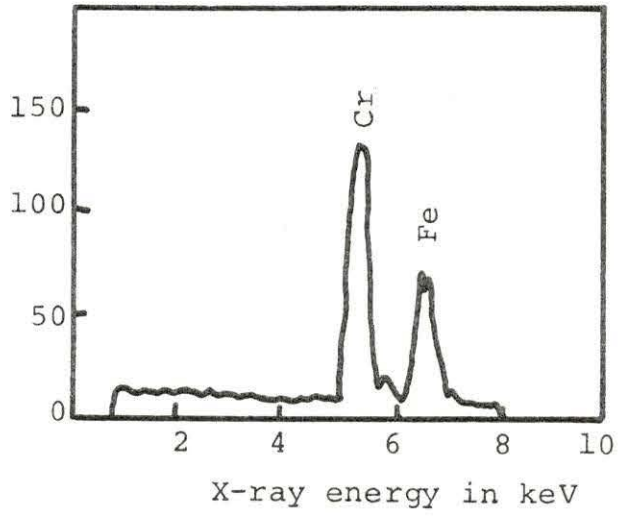
150
100
50
0
Cr
Fe
2
4
6
8
10
X-ray energy in keV

differences might be explained by the absorption of x-rays by other elements present. The materials are so similar that absorption affects will also be similar. Therefore absorption is not a reasonable explanation for the difference between this investigation and Russ and Kabaya's work. It is concluded that analysis of inclusions using the energy dispersive systems with detector resolution capabilities poorer than 330 eV are subject to complications which may prevent full utilization of the information generated, even if analyses are assembled for similar materials.

The SEM was also used to study topography. Two types of fracture surfaces were examined; 1) the plane of fracture surface perpendicular to the rolling direction and 2) the plane of fracture surface parallel to the rolling direction. Figures 13a and 13b are examples of fracture surfaces perpendicular and parallel to the rolling direction, respectively.

When discussing plastic deformation fracture, the fracture surface is usually described in terms of voids, dimples and particles. Voids are holes formed in the matrix material. During fracture each void is broken and forms two dimples.

In Figure 13a long lines of voids have grown together or coalesced to form one large, long void. These lines or strings of voids are parallel with the direction of rolling. The strings of voids are associated with strings of inclusions. These strings or clusters of inclusions were formed during the

Figure 13a. This SEM micrograph shows the fracture surface at low magnification. The rolling direction is parallel to the horizontal edge of the micrograph. The length of the scale bar is 50μm

Figure 13b. This SEM micrograph shows the difference in topography on a fracture surface when the rolling direction is parallel to the bar axis. The rolling direction is perpendicular to the plane of the micrograph. The length of the scale bar is 50μm

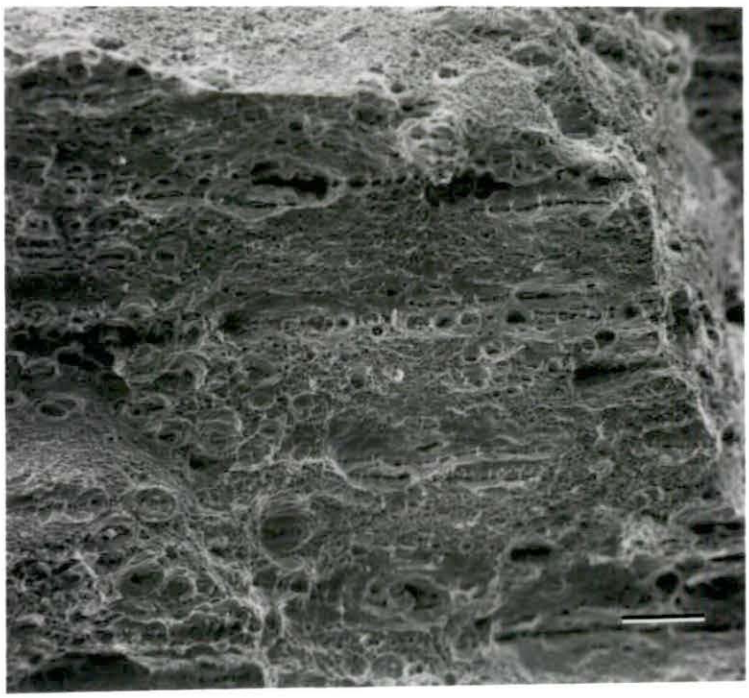

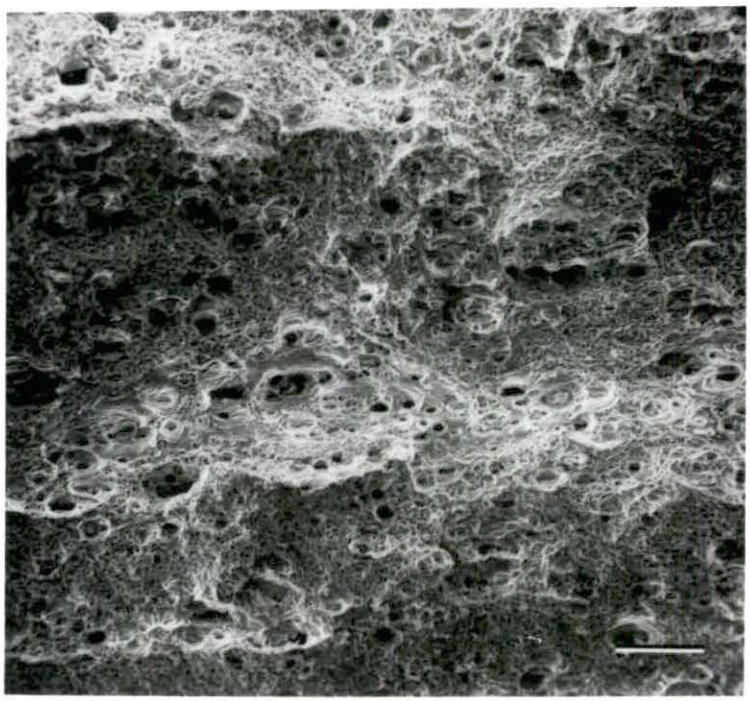

rolling process. The dimples are quite large around these particles. The outer edges of the dimples appear quite smooth compared with the rest of the matrix.

In Figure 13b, where the rolling direction is perpendicular to fracture surface, no long strings of voids are observed. The dimples are often grouped because during rolling, particles that are broken up will form clusters in a plane perpendicular to the rolling cluster. In Figure 13a there are some dimples that appear quite deep. This is due to the same effect. This, also, is due to clustering. Voids have coalesced in the fracture plane and also in the plane of the plate surfaces. There are some areas in Figure 13b where voids have coalesced but there is not as much coalescence as in Figure 13a. In each figure isolated voids appear to be elongated. This is due to the geometry of the sample bars and rolling effects. In both figures there exists a fine network of dimples filling in the area between larger voids. These dimples in the fine network are very similar to those observed by Russ and Kabaya (22). The dimples Russ and Kabaya observed were associated with chromium particles. The small dimples observed in this investigation showed some evidence of inclusions being associated with their formation. Inclusions were observed in a few of these smaller voids. There is a strong possibility that the inclusions that nucleated the voids were lost during actual fracture of the

bar. In many cases the inclusions are found in the walls of the voids rather than in the bottoms of the voids, indicating transport and possible detachment of inclusion material. At the actual point of fracture, it is observed that a small but distinguishable cloud of material is released.

Figures 14a and 14b assist in understanding the process of void coalescence of the larger voids. Figure 14a shows the stages of void coalescence for a string of particles. On the right hand side of the Figure a particle is seen in a dimple. The dimple has not yet grown together with the larger dimple to the left. The wall between the large dimple and the smaller dimple has started to separate or rupture. To the left of this region in the field of view there are examples of voids which have completely ruptured. Rupture ridges remain on the sides of the dimple. Figure 14b also shows clear evidence of void coalescence. There are rupture ridges on both sides of the dimple. Figure 10a shows an excellent view of rupture ridges. These mark the boundary or walls that once divided the particle seen in the dimples.

Figures 14a and 14b show several particles in these larger voids. There are two explanations for a number of particles in one dimple: 1) a large particle was broken earlier in the process of fracture and 2) many particles of the same cluster or group have formed these larger voids. The evidence of void coalescence in Figure 14b suggests the

Figure 14a. The SEM micrograph indicates the process of void coalescence for an area of a fracture surface. The rolling direction is parallel to the horizontal edge of the micrograph. The length of the scale bar is 2μm

Figure 14b. This SEM micrograph of a fracture surface shows the process of void coalescence. The rolling direction is parallel to the horizontal edge of the micrograph. The length of the scale bar is 2μm

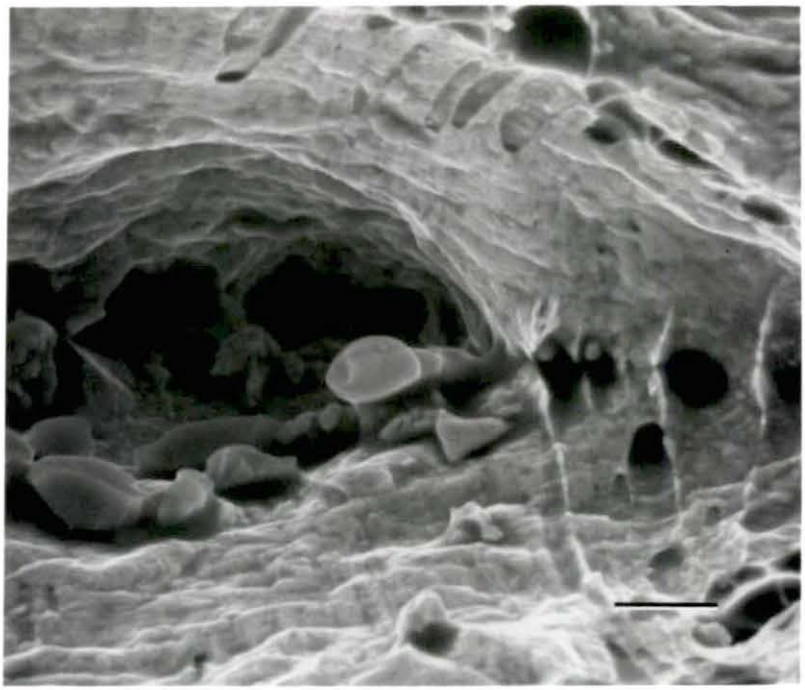

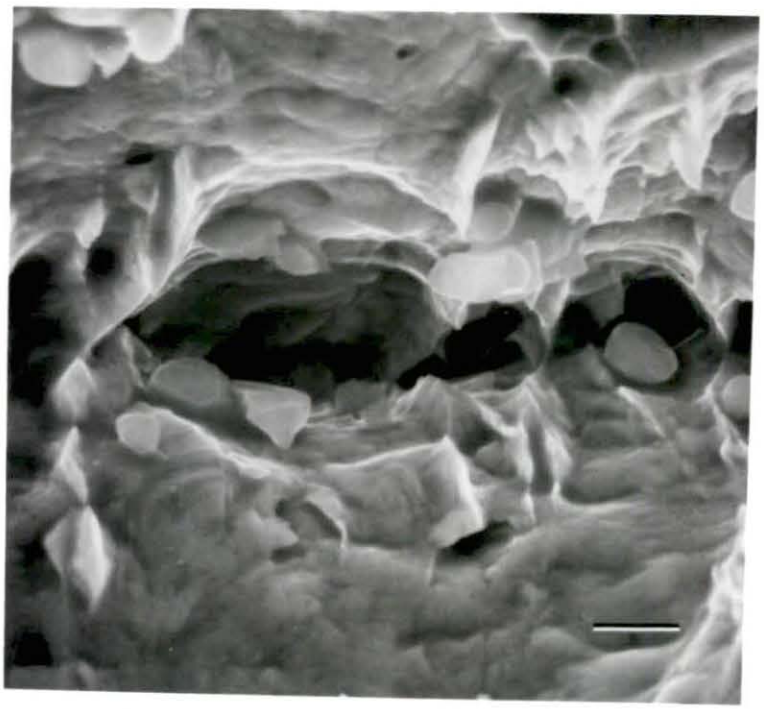

second explanation. However, there is evidence to support the first explanation in Figures 15a, 15b, and 9a as well. Figure 15b shows evidence of the inclusion-matrix bond being separated. There is also evidence of cracks in this particle. The mechanism of forming these cracks is cleavage fracture. Inclusions in Figure 15a and 9a appear to still be bonded to the matrix on the sides of each inclusion. The inclusion in 15a appears to have been pulled apart and broken in several places. From these micrographs the process of fracture by microvoid coalescence can be better understood.

By comparing and analyzing the results from microprobe and SEM measurements for the three stages of plastic deformation fracture, additional information was developed for characterizing the process of plastic fracture in Type 347ss. The identity of inclusions on the fracture surface was not accomplished with the 330 eV resolution energy dispersive system. In the future, a wavelength dispersive system could be used to identify inclusions on the fracture surface. The other possibility is to study some of the inconsistencies developed from results obtained from the energy dispersive analysis system. For example, why was nickel not detected in the matrix material and how large is the excitation volume of the x-rays?

Inclusions were identified with the microprobe on both deformed and undeformed samples. The partially deformed

Figure 15a. This SEM micrograph shows a fractured inclusion on a fracture surface. The rolling direction is parallel to the horizontal edge of the micrograph. The length of the scale bar is 2μm

Figure 15b. The SEM micrograph shows a fractured inclusion on a fracture surface. The rolling direction is the same as in the above micrograph. The length of the scale bar is 1μm

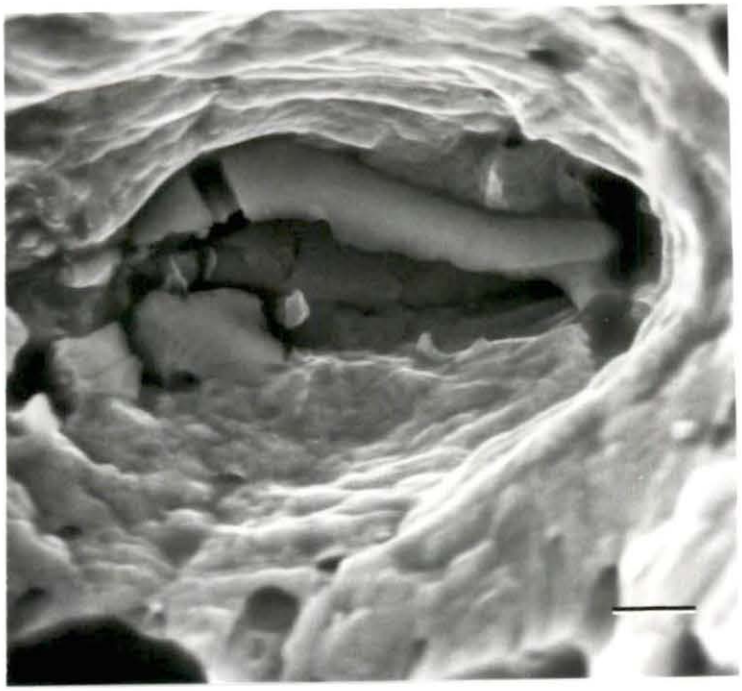

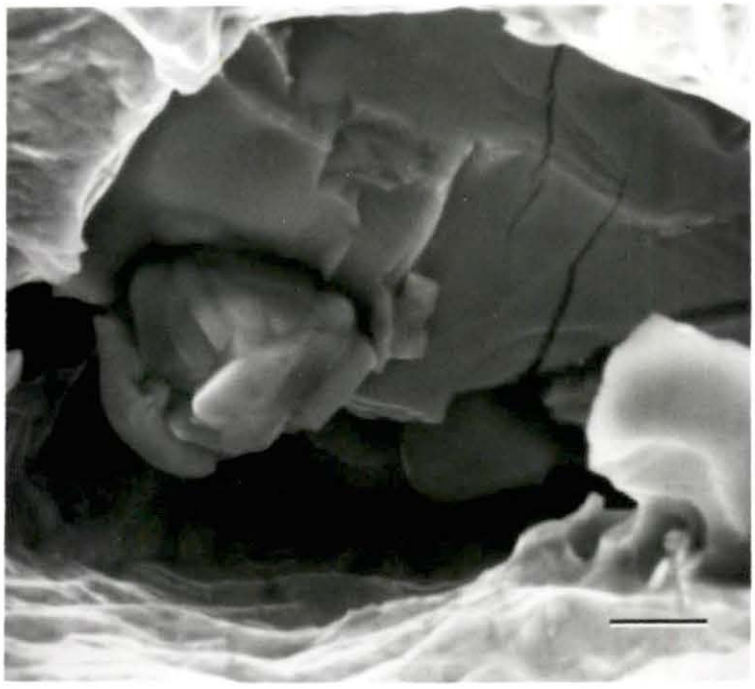

samples were most interesting. NbC particles were found to fracture during the early stages of necking and pre-necking. The fracture of these particles nucleated voids in the stainless steel. Their detrimental nature has been recognized. Some voids were found to be nucleated by MnS inclusions also. Generally, the MnS particles were smaller and therefore formed smaller voids. After void nucleation occurs, the next process is void coalescence.

Evidence of void coalescence is present in Figures 14a and 14b. In Figure 14b, ridges on each side of the dimple are present. These ridges are the remains of the rupture of the walls that once separated the voids earlier in the fracture process. In Figure 14a, coalescence is seen in several stages. On the left a group of voids have already coalesced. On the right side of the micrograph, dimples are shown in different stages of coalescence. Note ridges on each side of the dimples. Another possible mechanism of void coalescence is the formation of smaller voids which form a crack. This crack connects the larger particles. Limited evidence of this was observed on the fractures surfaces. In the upper central area of Figure 13a, there is a large dimple which has been formed due to the interconnection of large voids by forming a smaller network of voids. Void coalescence will be greatly enhanced if particles are closer to one another. An example of this is shown in Figures 13a and 11. The strings of

particles have formed voids which coalesced very easily because of their proximity to one another. This is the reason the bars were weaker when pulled with the rolling direction perpendicular to the pulling direction. In this situation the strings of particles would be perpendicular to the pulling direction. This is a weaker situation than when the strings are elongated in the pulling direction.

The next stage in fracture is an acceleration of void formation and coalescence, resulting in the fine network of dimples weakening the area between the larger voids and causing final failure. The tear dimples are parabolic in shape and represent the first evidence of this stage of fracture. Tear dimples are seen in Figures 9a and 15a.

CONCLUSIONS

Inclusions have been associated with the formation of large dimples. Due to the effects of rolling, large inclusions may fracture and form rows of smaller inclusions. These rows of small inclusions cause the formation of large voids also. The chemical identification of specific particles on the fracture surface was not accomplished. However, microprobe analysis established that the principle inclusions present in the specimens are MnS, NbC, and Al_2O_3. The mechanism of fracture was found to be microvoid formation, and is in general agreement with previous descriptions. The following details were learned about the process:

1) Larger inclusions and strings of inclusions were responsible for initial void formation.
2) Void coalescence of these larger voids occurred by necking down and rupturing of the walls between them, and in addition by smaller void formation.
3) Final fracture was accomplished catastrophically for remaining regions by small void formation. In some cases, these voids were seen to be related to the presence of small particles.
4) Particles as small as 1000 Å in diameter are recognized and contribute to the fracture observations. Present x-ray techniques (as well as other

analytical techniques) are not capable of yielding chemical identity information for these because of their very small size.

The rolling direction was found to be stronger because of the orientation of the stringers in the steel matrix. During void formation, void growth exhibited a higher degree of elongation for specimens where the rolling direction was parallel to the surface as compared to that for specimens where the rolling direction was perpendicular to the surface. The mechanism of smaller void formation is suspected to be the void sheet mechanism suggested by Rogers on the basis of studies of copper where he found void formation in the absence of inclusions. For these stainless steel specimens, attempts were made to determine if all the smaller voids were formed by inclusions; however, the evidence was not conclusive.

The SEM was found to be a very valuable tool for studies of fracture surfaces. The energy dispersive analysis results indicate that complex problems on element identification are present, and that preliminary information available in the literature was insufficient to predict this.

RECOMMENDATIONS FOR FUTURE STUDY

Considerably more information remains to be developed from SEM studies of fracture. This investigation has only developed a small portion of the information to be learned from studying plastic deformation fractures. This research was concerned with only one type of material and one type fracture. In future studies both the type of materials and the type of fracture could be varied. An example where this might be useful is related to the work of Rogers where his resolution limitation for recognizing particles was approximately 2μm in diameter. Since most of the stainless steel inclusions were 3μm or less in diameter, additional studies in the copper system would be appropriate. An important aspect of plastic deformation fracture still needs to be more fully developed, that of identification of particles found on a fracture surface.

REFERENCES

1. Tenenbaum, Michael. Nonmetallic Phases In Low-Carbon Sheet Steels of Various Origins. Transactions of the Metallurgical Society of AIME 245: 1675-1698. 1969.

2. Sims, Clarence E. The Nonmetallic Constituents of Steel. Transactions of Metallurgical Society of AIME 215: 367-392. 1959.

3. Kiessling, Roland and Nils Lange. Non-Metallic Inclusions in Steel. Vol. III. London, The Iron and Steel Institute. c1968.

4. Kiessling, Roland and Nils Lange. Non-Metallic Inclusions in Steel. Vol. II. London, Iron and Steel Institute. c1966.

5. Greaves, Richard Henry and Harold Wrighton. Practical Microscopical Metallography. London, Chapman and Hall Ltd. 1957.

6. Chao, H. C., L. H. Van Vlack, F. Oberin and L. Thomassen. Hardness of Inclusion Sulfides. ASM Transactions Quarterly 57: 885-891. 1964.

7. Brammar, I. S. and R. W. K. Honeycombe. Intergranular Brittleness of Cast Chromium-Nickel Steels. Journal of the Iron and Steel Institute 200: 1060-1067. 1962.

8. Brammar, I. S. and R. W. K. Honeycombe. Formation of Sulphides at Grain Boundaries in Some Pure Iron Alloys. Journal of the Iron and Steel Institute 202: 335-342. 1964.

9. Kiessling, Richard and Nils Lange. Non-Metallic Inclusions in Steel. Vol. I. London, The Iron and Steel Institute. c1964.

10. Linnert, George E. Welding Type 347 Stainless Steel Piping and Tubing. Welding Research Council Bulletin Series No. 43. 1958.

11. Szczepanski, M. The Brittleness of Steel. New York, John Wiley and Sons, Inc. c1963.

12. Shewmon, Paul G. Transformations in Metals. New York, McGraw-Hill Book Company. c1969.